

Influence of Manganese Doping on Optical Properties of Barium Ferrites Nanoparticles

A. H. AL-Hammadi ¹, Azmi A. M. Othman ¹, Sadiq. H. Khoreem ^{1,2,*} 

¹ Physics Department, Faculty of Science, Sana'a University, Sana'a, Yemen

² Dept. of Optometry and Vision Science, Faculty of Medical Sciences, Al-Razi University, Sana'a, Yemen

* Correspondence: khoreems@yahoo.com;

Scopus Author ID 57571836200

Received: 1.06.2022; Accepted: 7.07.2022; Published: 7.10.2022

Abstract: The barium hexaferrite magnetic materials Mn-doped $\text{BaZn}_{1+x}\text{Mn}_x\text{Fe}_{12-2x}\text{O}_{19}$ ($x = 0.4, 0.8, 1.2, 1.6,$ and 2) were prepared using the ceramic method. The powder samples ferrite were subjected to XRD, FT-IR, and UV-Vis to investigate the nanoparticles' structural changes. UV-Vis spectroscopy is used to obtain the samples' absorption spectrum and calculate the band gap energy. X-ray diffraction patterns and FT-IR investigations confirmed the formation of a single-phase M-type hexagonal structure. The grain size was measured from Scherrer's equation, and it is found in the range of 43-56 nm, with increasing the concentration of Mn ions, which shows the enhancement in the degree of crystallinity and increase in the size of grain size. UV-vis spectroscopy was used to confirm the formation of the $\text{BaZn}_{1+x}\text{Mn}_x\text{Fe}_{12-2x}\text{O}_{19}$ nanoparticles. The transmission was found to increase slowly in the 200-290 nm wavelength and then decreased to 332 nm after that increase until the maximum for all samples was about 99% in 480-800 nm wavelengths. The highest transmission will be exclusively used for window layers in solar cells. The band gap energy increased gradually with a rise in Mn ions and a decrease in Zn ion concentration. The refractive index, dielectric constant, and optical dielectric constant decreased with an increase in Mn ions and a decrease in Zn ions concentration.

Keywords: Mn-doping; structure; optical properties; ferrites; nanoparticles.

© 2022 by the authors. This article is an open-access article distributed under the terms and conditions of the Creative Commons Attribution (CC BY) license (<https://creativecommons.org/licenses/by/4.0/>).

1. Introduction

Nanotechnology research is becoming one of the most crucial fields due to its uniqueness and remarkable properties and rapidly expanding fields such as engineering, materials science, chemistry, physics, biology, and medicine. In particular, nanoscale ferrites are being investigated to enhance their structural, optical, electrical, and magnetic properties for to make them suitable for technological applications in catalysis, photoluminescence, humidity-sensors, photocatalysis, biosensors, magnetic drug delivery, permanent magnets, microwave absorbers, magnetic refrigeration water decontamination, antimicrobial agents, and biomedicine and other advanced electronic devices [1-5]. In recent years, researchers have been more interested in hexagonal ferrites. Different types of hexagonal ferrites, also famous as hexaferrite, have a long journey since their discovery [6]. Hence, an improvement in one of them is M-type ferrites, BaM, or barium ferrite ($\text{BaFe}_{12}\text{O}_{19}$). M-type hexagonal barium ferrite ($\text{BaFe}_{12}\text{O}_{19}$) with its rare earth doping elements such as neodymium (Nd) and samarium (Lanthanum substituted in M-type barium hexaferrite have attracted much interest due to its technological uses in permanent magnets and prospective applications in

high-density magnetic recording media, and barium hexaferrite is ideal for microwave devices due to its enormous crystalline anisotropy, huge magnetism, strong intrinsic coercivity, excellent chemical stability, high Curie temperature, and low price. [7]. Using synthetic techniques and doping different rare earth/transition metal ions in hexagonal configurations, ferrites' structural and electromagnetic properties can be adjusted [8]. Ferrites' inherent characteristics, such as permittivity, dielectric losses, and conductivity, are governed by their chemical makeup, annealing process, and kind of doped metal ions. [9]. One of the essential instruments for satisfying a wide range of uses is doping some suitable elements in the parent material. Zaheer Abbas Gilani et al. Effect and Microstructure Behavior of Rare-Earth Element Cerium (Ce^{+3}) in Barium Hexaferrite ($\text{BaCe}_x\text{Fe}_{12-x}\text{O}_{19}$). Nanoparticles Ferric (Fe^{+3}) sites can benefit from elemental replacements to increase their magnetic and dielectric characteristics.

Researchers discovered that barium hexaferrite doped with cerium (Ce^{+3}) has significantly improved microwave absorption properties, indicating that ($\text{BaCe}_x\text{Fe}_{12-x}\text{O}_{19}$) can be used in electronic components, high storage devices, and microwave technologies. [10]. Barium hexaferrite ($\text{BaZn}_x\text{Fe}_{12-x}\text{O}_{19}$) having zinc (Zn) as a substituent is prepared via the sol-gel method. Barium doped with a small concentration of Mn was investigated [11] as $\text{BaFe}_{12-x}\text{Mn}_x\text{O}_{19}$, where x was 0.5, 1.0, 1.5, and 2.0. The results showed that the coercivity was greater when the Mn concentration was larger. The lattice parameter a was constant while the c lattice parameter decreased. This means decreasing the lattice volume. Although much research has been reported on the structure, ferroelectric and magnetic properties of BaFeO nanoparticles by adjusting the Fe, Cr, Zn, Ce, and doping concentration, the optical properties require further investigation. The present work first grew the influence of Mn doping on the optical properties of $\text{BaZn}_{1+x}\text{Mn}_x\text{Fe}_{12-2x}\text{O}_{19}$ ($x = 0.4, 0.8, 1.2, 1.6, \text{ and } 2$). Barium ferrite nanoparticles are synthesized by the ceramic method. Then, the structures and optical properties of the samples were investigated. In particular, the impact of Mn doping on the structure and optical properties of the $\text{BaZn}_{1-x}\text{Mn}_x\text{FeO}_{19}$ nanoparticles ferrite were studied based on their absorption spectra. In this work, Investigations were conducted on the effects of Mn doping and zinc (zn) microstructure behavior in barium hexaferrite with the general formula $\text{BaZn}_{1+x}\text{Mn}_x\text{Fe}_{12-2x}\text{O}_{19}$ ($x = 0.0, 0.4, 0.8, 1.2, 1.6, \text{ and } 2$). The prepared ferrite material is characterized by x-ray diffraction (XRD), Fourier transform infrared spectroscopy (FTIR), and UV-Visible spectroscopy properties analysis.

2. Materials and Methods

Highly pure BaCO_3 , MnO , ZnO , and Fe_2O_3 to produce a sequence of polycrystalline M-type hexagonal nano ferrites in the correct ratio, manganese (Mn^{+2}) doped barium hexaferrite with compositional formula $\text{BaZn}_{1+x}\text{Mn}_x\text{Fe}_{12-2x}\text{O}_{19}$ (Where $x = 0.0, 0.4, 0.8, 1.2, 1.6 \text{ and } 2$) was prepared by using the ceramic method, as mentioned before [12]. First, the mixed oxides powders were ground for six hours using an agate mortar for 10 h. The powders mixture was air-dried. The powders were then presintered for 8 hours at 950 K. The grain powders were cooled to room temperature gradually. The characterization of samples has been performed using different analytical methods such as (XRD, FT-IR, and UV) [12]. The crystal structure and phase purity of Mn-substituted $\text{BaZn}_{1+x}\text{Mn}_x\text{Fe}_{12-2x}\text{O}_{19}$ powder samples have been investigated using X-ray diffraction (XRD) with $\text{Cu-K}\alpha$ radiation of 1.5406 \AA (Shimadzu EDX-720). FT-IR spectra fine powder for all compositions have been recorded in the range of $400 \text{ to } 1000 \text{ cm}^{-1}$, and measurements were made at room temperature (Perkin-Elmer (Model 783) spectro-meter using with KBr as solvent.

3. Results and Discussion

3.1. XRD analysis.

In order to confirm the phase formation of BaZn_{1+x}Mn_xFe_{12-2x}O₁₉ with compositions (0, 0.4, 0.8, 1.2, 1.6, and 2) nanoparticles, an XRD study is carried out for all prepared samples. It can be observed in Figure 1a. XRD measurements showed that all samples with Mn doping have a typical structure and exhibit a single phase of M-type hexagonal structure. The impact of Mn²⁺ substitution on the lattice parameters, unit cell volume, and crystal size of sample ferrites has been studied.

The lattice constant of hexagonal structures is computed using the relation (1) [13]:

$$\frac{1}{d_{hkl}^2} = \frac{4}{3} \frac{h^2 + hk + k^2}{a^2} + \frac{l^2}{c^2} \quad (1)$$

By using Scherrer's equation 2, [14], the average crystallite sizes (D) have been calculated from all high-intensity peaks of the XRD pattern and listed in Table 1:

$$D = \frac{0.9 \lambda}{\beta \cos \theta} \quad (2)$$

where 'D' is the average grain size, 0.9 is the shape factor, λ is the wavelength of X-ray, which is equal to λ = 1.541874 Å, β represents the peak at half maximum width, while 2θ denotes the diffraction angle.

With an increase in the Mn doping concentration, a small reduction in the average crystallite size was found within the range of 43.97–52.03 nm, as shown in Table 1. It is observed that with the rise of Mn content, the crystallite size also decreases. Materials with less than 60 nm crystallite size are generally considered good materials to obtain a high signal-to-noise ratio for high-density recording media [15]. The results for all synthesis samples are summarized in table 1. The lattice constants and the unit cell volume for the Mn-doped nanoparticles ferrite are slightly smaller than the pure BaZnFe₁₂O₁₉ and tend to decrease with increasing the Mn doping; this decrease is attributed to the small distinction of ionic radii.

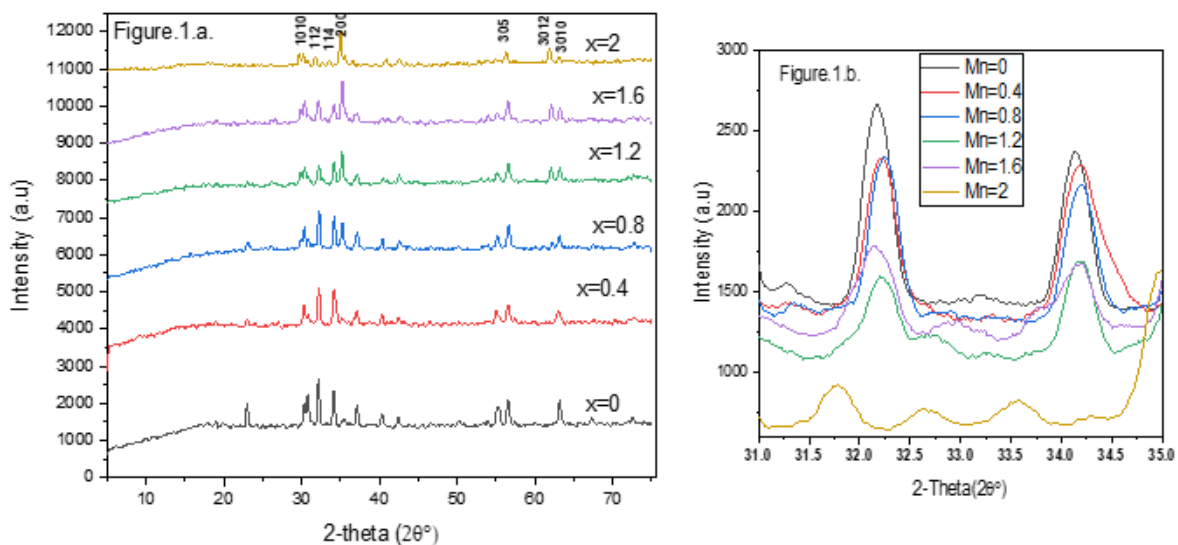


Figure 1. (a). X-ray diffraction patterns of BaZn_{1+x}Mn_xFe_{12-2x}O₁₉; (b) Peak shift for BaZn_{1+x}Mn_xFe_{12-2x}O₁₉.

Therefore, this decrease was owing to the smaller ionic radius of Fe³⁺ (0.64 Å) and Zn (0.74 Å) than Mn²⁺ (0.80 Å). The unit cell volume also is disposed to decrease with the increase of the Mn doping concentration. Usually this can often be a result of the distinction in radius caused by ion substitution created by the a- and c-axes undergoing distinct alterations. The intensity peaks observed changed with increasing Mn ions substitution doped, which moves slightly towards the higher angle, as shown in Figure 1b. This slight shift was a result of cationic replacement by larger ionic radii Mn²⁺ (0.80 Å) into smaller ionic radii Fe³⁺ (0.64 Å) and Zn (0.74 Å). This proportional variation indicated the BaZn-Mn ferrite system agreement of Vegard's law [14].

Table 1. X-ray density (ρ_x), bulk density (ρ_b), lattice constants (a, c), volume (v), grain size.

x=	ρ_x (g/cm ³)	ρ_b (g/cm ³)	A (nm)	c (nm)	V (cm ³)	grain size (nm)
0	5.563	4.807	5.899	23.306	702.4033	52.038
0.4	5.585	4.556	5.901	23.261	701.6789	49.9551
0.8	5.621	4.546	5.895	23.233	699.2577	51.2875
1.2	6.238	4.843	5.791	21.588	627.1789	46.886
1.6	6.300	5.577	5.7886	21.625	627.577	48.0628
2	6.149	5.375	5.800	22.133	644.869	43.9735

The X-ray density (ρ_x) was calculated by using equation 3:

$$\rho_x = \frac{ZM}{N_A V_{cell}} \tag{3}$$

where, M represents the molecular mass of samples, Z denotes the number of molecules per unit cell, and NA is Avogadro's number.

The calculated values of x-ray density ρ_x are listed in Table 1. The result showed that the x-ray density behavior was noticed that with the increase of Mn dopant concentration, the x-ray density value increased. This increase depends on the molecular weight of the sample

Bulk density (ρ_b) was estimated by using the following equation (4):

$$\rho_b = \frac{m}{\pi r^2 h} \tag{4}$$

where 'm' is the mass of the pellet, 'h' is the thickness, and 'r' is the radius.

The values of bulk density were low as compared to X-ray density.

3.2. Fourier transform infrared (FTIR) analysis.

Figure 2 shows the plots of infrared spectra of Mn substituted BaZn_{1+x}Mn_xFe_{12-2x}O₁₉ ferrite. The spectra were recorded at room temperature in the frequency range of 400–1000 cm⁻¹. Two frequency bands confirmed the higher frequency band (ν_1) (571–599 cm⁻¹) and lower frequency band (ν_2) (434–464 cm⁻¹) are assigned to the tetrahedral and octahedral sites, respectively [16, 17]. To be clear from Figure 2 show the single hexagonal structure with the formation of two kinds of characteristic absorption bands. Thus, the formation of a single-phase hexagonal structure of ferrites was confirmed to clear the hexagonal structure with the formation of two kinds of characteristic absorption bands found at around 434–460 cm⁻¹ and 571–599 cm⁻¹. These were associated with the stretching vibrations of tetrahedral (A-site) and octahedral (B-site) sites, respectively [18].

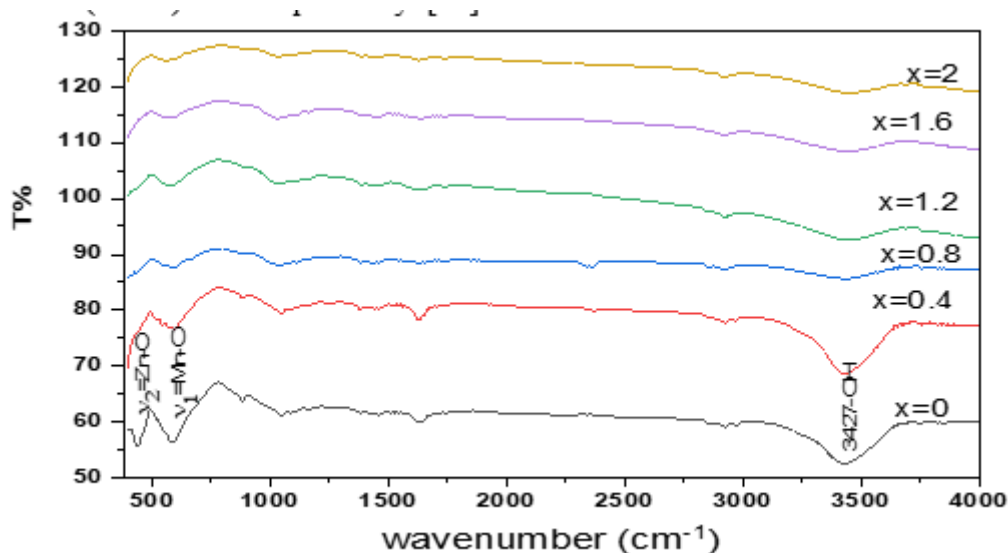


Figure 2. Observed and calculated FT-IR spectra for $\text{BaZn}_{1+x}\text{Mn}_x\text{Fe}_{12-2x}\text{O}_{19}$.

It can be observed from the IR plots that the band positions and changes slightly. This may be due to the distribution of Mn ions (ionic radius 0.64 \AA) which are replacing Fe^{3+} ions (ionic radius of 0.67 \AA) at the octahedral [B] site; thus, making some changes in the size of the tetra- and octahedron. It can be seen that the frequency shifted to higher frequencies with increasing Mn content, and the values of frequency bands are shown in figure 2. The fluctuation in the cation-oxygen bond length of the spinel's octahedral lattice may be the cause of the shift in band locations that occurs when the Mn content is increased. The displacement of Fe^{3+} ions by smaller Mn ions will result in a somewhat decrease in the metal-oxygen bond length and consequently will increase the wave number of bands. The band's splitting into bands of medium intensity may be logically attributed to the increasing quantity of the $\text{Mn}^{2+} - \text{O}_2$ -complexes as the Fe^{3+} content decreases at the B-site. The broad absorption in the $3350\text{--}3650 \text{ cm}^{-1}$ range is attributed to the $-\text{OH}$ groups of H_2O , indicating the existence of water absorbed on the surface of ZnO nanograins.

3.3. Optical study.

The bandgap energy and, therefore, the optical property of the as-prepared material were measured by using a UV-Visible spectrometer at room temperature within the wavelength range of 200 to 800 nm. The optical absorption of the ferrite nanoparticles is very important because of the UV-vis absorption edge, which is related to the band gap energy of the photocatalyst. Figure 3a and Figure 2b show the variation of transmission and optical absorption spectra with wavelength, respectively. The transmission is found to increase slowly in the 200-290 nm wavelength and then decrease to 332 nm after that increase until the maximum for all samples is about 99% in 480-800 nm wavelengths. Therefore, it shows the highest transmission performance because of less light scattering and will be exclusively used for window layers in solar cells [19]. Then for higher dopants in Mn, the surface texture modified towards increased roughness, voids presence, lattice distortion, and increased residual stress, as noticed in XRD results. Hence, the increased scattering of photons by crystal defects in samples could also be attributed to the reduction of optical transmittance [20].

Besides, defects within the microstructure strongly influence the transmission of the nanoparticles and, therefore, aligns with the study of Sahu et al. [21].

A distinction within the absorption edge was observed with Mn dopants concentration. A sharp absorption edge has been observed at around 334 nm. As Mn dopant concentration increased, significant red shifting of absorption edge has been observed towards the upper wavelength at 334 to 336 nm range as shown in figure 3b. These shiftings are because of the enhanced lower band gap indicator for these doped samples. It was found that the absorbance initially decreased sharply and then decreased gradually for all the samples in the visible range. The decrease in absorbance with doping could also be attributed to the decrease in the size of nanoparticles that ultimately widens the bandgap [22]. The band gap energy has been calculated from the spectrum absorption data by using the Tauc plot relation as follows in equation 5 [13]:

$$\alpha = \frac{A(h\nu - E_g)^n}{h\nu} \tag{5}$$

where, $h\nu$ is the incident photon energy, A is constant; therefore, the band gap has been calculated by extrapolating the linear region of the plots $(\alpha h\nu)^2$ versus $h\nu$ on the energy axis. The band gap values concluded from the graph range of 2.85 eV to 3.07 eV. The variation of band gap energy with Zn ions substitution is depicted in Figure 4 and Table 2. Figure 4 shows that the energy band gap increases with increased zinc ions substitution. The energy band gap value increase is attributed to the quantum confinement phenomenon at the nano-regime. Quantum confinement at the nanoscale plays a vital role in increasing the band gap. Several properties, like the size of the particles, a dopant, absorption coefficient, and preparation methods, affect the material's optical band gap. The material, which includes a high band gap, is helpful for solar cell applications [23]. The optical band gap significantly increased for all samples. Such increase in the optical band gap with increasing Mn dopant concentration where an enhancement of n-type carrier concentration occurred in $\text{BaZn}_{1+x}\text{Mn}_x\text{Fe}_{12-2x}\text{O}_{19}$, structure due to (Fe^{3+} doping) will be well explained by Burstein–Moss effect [24]. These effects show that with the increase of n-type carrier concentration with doping, absorption edge forms at much shorter wavelengths than intrinsic samples and lowers the fermi level down into the conduction band, which increases the band gap. This can be well-known as Burstein–Moss effect. The band gap energy is shown in table 2, which increases gradually with the increase of the Mn concentration percent. The bandwidth of conduction and valance bands increased as the manganese concentration increased, resulting in a band gap. In addition, the band gap values increase with increases in Mn concentrations which means the energy levels within the bands are increased in which each electron requires less energy to jump from the valance band to the conduction band.

3.4. Refractive index (n).

The index of refraction (n) of samples doped with Zn ions was calculated by using equation 6 [13]:

$$n = [(1+R)/(1-R)] + [(4 \times R)/(1-R)^2 - k^2]^{1/2} \tag{6}$$

where, R is the coefficient of reflection and k is the extinction coefficient.

The refractive index showed a decrease from 2.948 to 1.563 with Mn^{2+} ions concentration increase, as shown in Table 3. The effects of large ionic size and concentration

of Zn²⁺ ions may be responsible for the decrease. The same behavior was reported by [13, 25]. This could result in substituting Mn and Fe with Zn ions with higher polarizability.

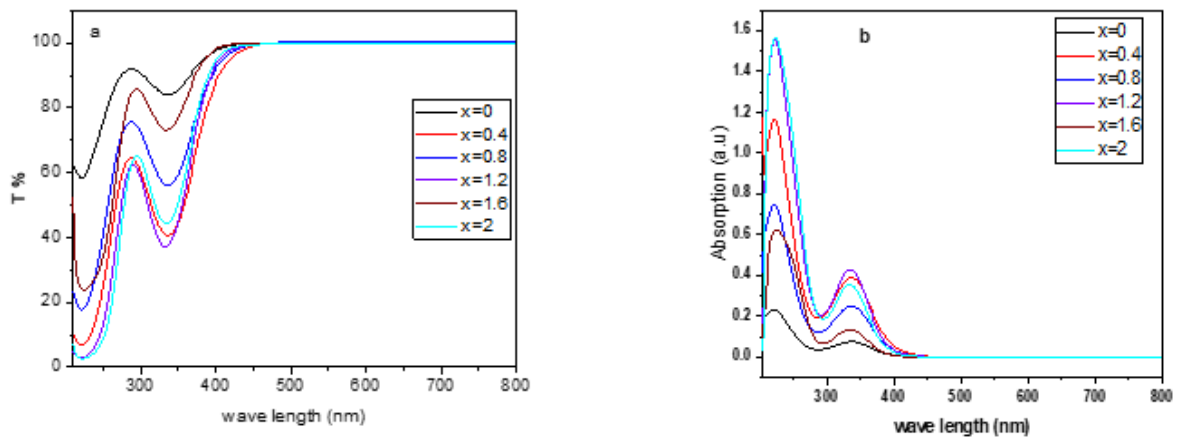


Figure 3. (a) Transmittance (T%) as a function of wavelength; (b) Absorption as a function of wavelength.

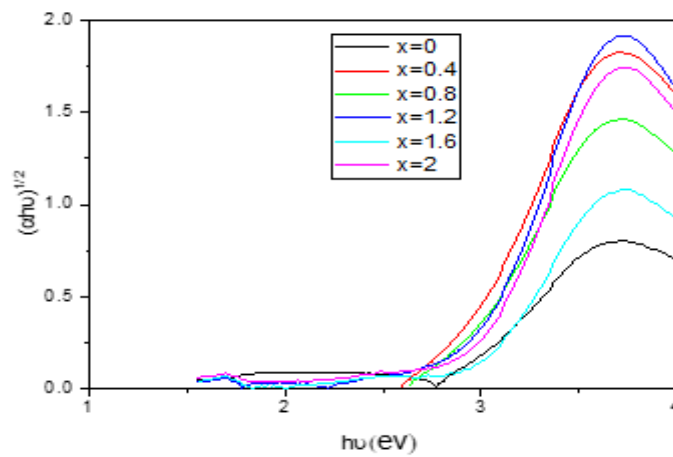


Figure 4. Band gap of BaZn_{1+x}Mn_xFe_{12-2x}O₁₉ ferrites nanocomposites.

Table 2. The optical band gap of BaZn_{1+x}Mn_xFe_{12-2x}O₁₉ ferrites nanocomposites.

Sample	Mn Concentration	Bandgap (ev)
BaZn Fe10O19	0	2.85 ev
BaZn1.4Mn0.4Fe11.2O19	0.4	2.807 ev
BaZn1.8Mn0.8Fe10.2O19	0.8	2.84 ev
BaZn2.2Mn1.2Fe9.6O19	1.2	2.96 ev
BaZn2.4Mn1.6Fe8.8O19	1.6	3.07 ev
BaZn3Mn2Fe8O19	2	2.978 ev

3.5. Dielectric constant.

The dielectric function (constant) is directly associated with the energy band gap, and therefore, the dielectric constant during this work was obtained using the formula reported by [26]:

$$\varepsilon = n^2 \tag{7}$$

3.6. Optical dielectric constant.

The relationship between the optical dielectric constant and the refractive index, polarization (p), and the static dielectric, as reported by [27], was used:

$$\epsilon = p \frac{dp}{dt} = \epsilon - 1 = n^2 - 1 \tag{8}$$

The dielectric and optical dielectric constants, as given in table 3. decreased from 8.691 to 2.444 and 7.691 to 1.444, respectively, with an increase in the concentration of Mn ions. The decrease in the value of the two dielectric constants, as shown in Table 3, indicates a decrease in the optical absorption and extinction coefficient of the samples with increasing Mn ions concentration.

Table 3. Zinc ion concentration, Refractive index (n), energy band gap (E), dielectric constant (ϵ), optical dielectric constant (ϵ_{opt}) of the Mn-doped $BaZn_{1+x}Mn_xFe_{12-2x}O_{19}$.

Mn	n	$\epsilon = n^2$	$\epsilon_{opt} = n^2 - 1$
0	2.948	8.691	7.691
0.4	2.803	7.858	6.858
0.8	2.665	7.102	6.102
1.2	2.268	5.1439	4.143
1.6	1.824	3.327	2.327
2	1.563	2.444	1.444

4. Conclusions

The $BaZn_{1+x}Mn_xFe_{12-2x}O_{19}$ ($x = 0.0, 0.4, 0.8, 1.2, 1.6,$ and 2) composition doped by Mn ions has been successfully synthesized using ceramic. The structural studies are done using XRD, UV, and FT- IR techniques. The X-ray diffraction investigations performed at room temperature confirmed the formation of a single-phase hexagonal structure and indicated the influence of Mn^{2+} substitution on the sample structure. For the samples, the range of the average crystallite size is 43–56 nm. The M-hexagonal structure of ferrites was confirmed from FT-IR with the formation of two kinds of characteristic absorption bands found at around 434-460 cm^{-1} and 571-599 cm^{-1} . These were associated with the stretching vibrations of tetrahedral (A-site) and octahedral (B-site) sites, respectively and the frequency bands shifted to higher frequencies with increasing Mn content. The absorbance of the sample was measured by UV spectroscopy. The transmission was found to be increased slowly in the 200-290 nm wavelength and then decreased to 332 nm after that increase until the maximum for all samples was about 99% in 480-800 nm wavelengths. The highest transmission will be exclusively used for window layers in solar cells. The energy band gap increases gradually with the increase of dopant sample concentration. The increase in the band gap value is attributed to the quantum confinement phenomenon taking place at the nano-regime. The bandwidth of conduction and valance bands increase as the concentration of Mn ions increases, which results in a band gap, The material which includes a high band gap is helpful for solar cell application. While the refractive index, dielectric constant, and optical dielectric constant decreased with increasing concentration of Mn ions.

Funding

This research received no external funding.

Acknowledgments

The authors appreciate the reviewers' contribution to improving the paper's quality. The authors are most grateful to the head of the Physics Department at the Faculty of Sciences, Sana'a University -Yemen. The authors are thankful to the UV and FT-IR laboratory team in the <https://biointerfaceresearch.com/>

Chemistry Department for providing their lab to carry out the present work. (Dr. Adliah & research assistant: Monther. A. Al-Hakemi).

Conflicts of Interest

The authors declare no conflict of interest.

References

1. Dippong, T.; Levei, E.A.; Cadar, O. Recent Advances in Synthesis and Applications of MFe_2O_4 ($M = Co, Cu, Mn, Ni, Zn$). *Nanomaterials* **2021**, *11*, 1560, <https://doi.org/10.3390/nano11061560>.
2. Asghar, K.; Qasim, M.; Das, D. Preparation and Characterization of Mesoporous Magnetic $MnFe_2O_4@mSiO_2$ Nanocomposite for Drug Delivery Application. *Materials Today: Proceedings* **2020**, *26*, 87–93, <https://doi.org/10.1016/j.matpr.2019.05.380>.
3. Dippong, T.; Levei, E.A.; Cadar, O. Formation, Structure and Magnetic Properties of $MFe_2O_4@SiO_2$ ($M = Co, Mn, Zn, Ni, Cu$). *Materials* **2021**, *14*, 1139, <https://doi.org/10.3390/ma14051139>.
4. Thakur, P.; Chahar, D.; Taneja, S.; Bhalla, N.; Thakur, A. A Review on MnZn Ferrites: Synthesis, Characterization and Applications. *Ceramics International* **2020**, *46*, 15740–15763, <https://doi.org/10.1016/j.ceramint.2020.03.287>.
5. Jabbar, R.; Sabeeh, S.H.; Hameed, A.M. Structural, Dielectric and Magnetic Properties of Mn^{+2} Doped Cobalt Ferrite Nanoparticles. *Journal of Magnetism and Magnetic Materials* **2020**, *494*, 165726, <https://doi.org/10.1016/j.jmmm.2019.165726>.
6. Sharma, G.; Kumar, A.; Dhiman, P (Eds). *Ferrite: Nanostructures with Tunable Properties and Diverse Applications*. Material Research Forum LLC **2021**, <http://dx.doi.org/10.21741/9781644901595>.
7. Chugh, M., Basandrai, D. Investigation of Rare Earth Element Inclusion on the Structural and Magnetic Properties of Barium Ferrites. In: Verma, P., Samuel, O.D., Verma, T.N., Dwivedi, G. (eds) *Advancement in Materials, Manufacturing and Energy Engineering* **2022**, vol. II. Lecture Notes in Mechanical Engineering. Springer, Singapore, https://doi.org/10.1007/978-981-16-8341-1_1.
8. Liu, J.; Feng, X.; Wu, S.; Zhou, P.; Huang, J.; Li, H.; Liang, T. High Microwave Absorption Performance in Nd-Substituted BaM/GO through Sol-Gel and High Energy Ball Milling Process. *Journal of Alloys and Compounds* **2022**, *892*, 162207, <https://doi.org/10.1016/j.jallcom.2021.162207>.
9. Almessiere, M.A.; Slimani, Y.; Güngüneş, H.; Demir Korkmaz, A.; Trukhanov, S.V.; Guner, S.; Alahmari, F.; Trukhanov, A.V.; Baykal, A. Correlation between Chemical Composition, Electrical, Magnetic and Microwave Properties in Dy-Substituted Ni-Cu-Zn Ferrites. *Materials Science and Engineering: B* **2021**, *270*, 115202, <https://doi.org/10.1016/j.mseb.2021.115202>.
10. Gilani, Z.A.; Ahmed, A.; Asghar, H.M.N.; Khalid, M. Doping Effect and Microstructure Behavior of Rare-Earth Element Cerium (Ce^{+3}) in Barium Hexaferrite ($BaCe_xFe_{12-x}O_{19}$) Nanoparticles. *Journal of Materials and Physical Sciences* **2020**, *1*, 58–77, <https://doi.org/10.52131/jmps.2020.0102.0007>.
11. Sharma, P.; Rocha, R.A.; de Medeiros, S.N.; Paesano, A.; Hallouche, B. Structural, Mössbauer and Magnetic Studies on Mn-Substituted Barium Hexaferrites Prepared by High Energy Ball Milling. *Hyperfine Interact.* **2008**, *175*, 77–84, <http://dx.doi.org/10.1007/s10751-008-9591-2>.
12. Al-Hammadi, A.H.; Khoreem, S.H. Investigations on Optical and Electrical Conductivity of Ba/Ni/Zn/Fe₁₆O₂₇ Ferrite Nanoparticles. *Biointerface Res Appl Chem* **2022**, *13*, 168, <http://dx.doi.org/10.33263/BRIAC132.168>.
13. Al-Hammadi, A.H.; Khoreem, S.H. Influence of Zn⁺² Doping on Dielectric Properties of Ba-Based Nanoferrites. *Biointerface Res Appl Chem.* **2022**, *13*, 265, <http://dx.doi.org/10.33263/BRIAC133.256>.
14. Massit, A.; El Yacoubi, A.; Kholtei, A.; El Idrissi, B.C. XRD and FTIR Analysis of Magnesium Substituted Tricalcium Calcium Phosphate Using a Wet Precipitation Method. *Biointerface Res Appl Chem* **2020**, *11*, 8034–8042, <http://dx.doi.org/10.33263/BRIAC111.80348042>.
15. Zhang, W.; Li, P.; Wang, Y.; Guo, J.; Li, J.; Shan, S.; Ma, S.; Suo, X. Structure, Spectra, Morphology, and Magnetic Properties of Nb⁵⁺ Ion-Substituted Sr Hexaferrites. *Magnetochemistry* **2022**, *8*, 51, <https://doi.org/10.3390/magnetochemistry8050051>.
16. Chukanov, N.V. *Infrared Spectra of Mineral Species: Extended Library*. Springer Science + Business Media Dordrecht **2014**, <https://doi.org/10.1007/978-94-007-7128-4>.
17. Islam, R.; Hakim, M.A.; Rahman, M.O.; Narayan Das, H.; Mamun, M.A. Study of the Structural, Magnetic and Electrical Properties of Gd-Substituted Mn–Zn Mixed Ferrites. *Journal of Alloys and Compounds* **2013**, *559*, 174–180, <https://doi.org/10.1016/j.jallcom.2012.12.080>.
18. Desai, K.R.; Alone, S.T.; Wadgane, S.R.; Shirsath, S.E.; Batoo, K.M.; Imran, A.; Raslan, E.H.; Hadi, M.; Ijaz, M.F.; Kadam, R.H. X-Ray Diffraction Based Williamson–Hall Analysis and Rietveld Refinement for Strain Mechanism in Mg–Mn Co-Substituted CdFe₂O₄ Nanoparticles. *Physica B: Condensed Matter* **2021**, *614*, 413054, <https://doi.org/10.1016/j.physb.2021.413054>.
19. Fang, Z.; Zhu, H.; Yuan, Y.; Ha, D. et al. Novel Nanostructured Paper with Ultrahigh Transparency and

- Ultrahigh Haze for Solar Cells. *Nano Lett.* **2014**, *14*, 765–773, <https://doi.org/10.1021/nl404101p>.
20. Sakka, S. History of Ferroelectric Materials Prepared by Sol-Gel Method. *J. of Sol-Gel Science and Technology* **2022**, *101*, 140–175, <https://doi.org/10.1007/s10971-021-05712-w>.
 21. Sahu, J.; Soni, S.; Kumar, S.; Dalela, B.; Alvi, P.A.; Sharma, S.S.; Phase, D.M.; Gupta, M.; Kumar, S.; Dalela, S. Defects and Oxygen Vacancies Tailored Structural, Optical and Electronic Structure Properties of Co-Doped ZnO Nanoparticle Samples Probed Using Soft X-Ray Absorption Spectroscopy. *Vacuum* **2020**, *179*, 109538, <https://doi.org/10.1016/j.vacuum.2020.109538>.
 22. Möbs, J.; Luy, J.-N.; Shlyaykher, A.; Tonner, R.; Heine, J. The Influence of Copper on the Optical Band Gap of Heterometallic Iodido Antimonates and Bismuthates. *Dalton Trans.* **2021**, *50*, 15855–15869, <https://doi.org/10.1039/D1DT02828F>.
 23. Zarhri, Z.; Cano, A.D.; Oubram, O.; Ziat, Y.; Bassam, A. Optical Measurements and Burstein Moss Effect in Optical Properties of Nb-Doped BaSnO₃ Perovskite. *Micro and Nanostructures* **2022**, *166*, 207223, <https://doi.org/10.1016/j.micrna.2022.207223>.
 24. Eevon, C.; Halimah, M.K.; Zakaria, A.; Azurahaman, C.A.C.; Azlan, M.N.; Faznny, M.F. Linear and Nonlinear Optical Properties of Gd³⁺ Doped Zinc Borotellurite Glasses for All-Optical Switching Applications. *Results in Physics* **2016**, *6*, 761–766, <https://doi.org/10.1016/j.rinp.2016.10.010>.
 25. Linda, D.; Duclère, J.-R.; Hayakawa, T.; Dutreilh-Colas, M.; Cardinal, T.; Mirgorodsky, A.; Kabadou, A.; Thomas, P. Optical Properties of Tellurite Glasses Elaborated within the TeO₂-Tl₂O-Ag₂O and TeO₂-ZnO-Ag₂O Ternary Systems. *Journal of Alloys and Compounds* **2013**, *561*, 151–160, <https://doi.org/10.1016/j.jallcom.2013.01.172>.
 26. LIM, Seung-Gu, et al. Dielectric functions and optical bandgaps of high-K dielectrics for metal-oxide-semiconductor field-effect transistors by far ultraviolet spectroscopic ellipsometry. *Journal of applied physics*, **2002**, *91.7*: 4500-4505. <https://aip.scitation.org/doi/abs/10.1063/1.1456246>.
 27. Najar, F.A.; Abass, S.; Sultan, K.; Kharadi, M.A.; Malik, G.F.A.; Samad, R. Comparative Study of Optical Properties of Substitutionally Doped La₂NiMnO₆ Double Perovskite Ceramic: A Potential Candidate for Solar Cells and Dielectrics. *Physica B: Condensed Matter* **2021**, *621*, 413311, <https://doi.org/10.1016/j.physb.2021.413311>.